J. Fluid Mech. (2002), *vol.* 465, *pp.* 33–58.
DOI: 10.1017/S0022112002008893 Printed in the United Kingdom

Modulated rotating waves in an enclosed swirling flow

By H. M. BLACKBURN[1] AND J. M. LOPEZ[2]

[1]CSIRO Building, Construction and Engineering, P.O. Box 56, Highett, Vic 3190, Australia

[2]Department of Mathematics, Arizona State University, Tempe, AZ 85287-1804, USA

(Received 24 July 2001 and in revised form 2 February 2002)

The loss of axisymmetry in a swirling flow that is generated inside an enclosed cylindrical container by the steady rotation of one endwall is examined numerically. The two dimensionless parameters that govern these flows are the cylinder aspect ratio and a Reynolds number associated with the rotation of the endwall. This study deals with a fixed aspect ratio, height/radius = 2.5. At low Reynolds numbers the basic flow is steady and axisymmetric; as the Reynolds number increases the basic state develops a double recirculation zone on the axis, so-called vortex breakdown bubbles. On further increase in the Reynolds number the flow becomes unsteady through a supercritical Hopf bifurcation but remains axisymmetric. After the onset of unsteadiness, another two unsteady axisymmetric solution branches appear with further increase in Reynolds number, each with its own temporal characteristic: one is periodic and the other is quasi-periodic with a very low frequency modulation. Solutions on these additional branches are unstable to three-dimensional perturbations, leading to nonlinear modulated rotating wave states, but with the flow still dominated by the corresponding underlying axisymmetric mode. A study of the flow behaviour on and bifurcations between these solution branches is presented, both for axisymmetric and for fully three-dimensional flows. The presence of modulated rotating waves alters the structure of the bifurcation diagram and gives rise to its own dynamics, such as a truncated cascade of period doublings of very-low-frequency modulated states.

1. Introduction

The flow that is produced inside a stationary cylindrical cavity by the steady rotation of one endwall has served as the basis of many investigations into the fundamentals of swirling flows. When the flow is incompressible and the fluid Newtonian, the two dimensionless groups that characterize the system are the cylinder aspect ratio $\Lambda = H/R$, where H and R are respectively the height and radius of the cylinder, and the Reynolds number $Re = \Omega R^2/\nu$, where Ω is the rotational speed of the moving endwall and ν is the kinematic viscosity of the fluid. A schematic of the flow is presented in figure 1, with an inset showing contours of streamfunction for a typical basic state, which is steady and axisymmetric. The flow is driven by the rotation of the bottom endwall, setting up an Ekman layer that centrifuges fluid radially outwards. The stationary sidewall of the cylinder diverts this flow into the axial (vertical) direction, turning the Ekman layer into a shear layer that is inclined slightly in from the sidewall and that has jet-like velocity profiles in both the azimuthal and axial

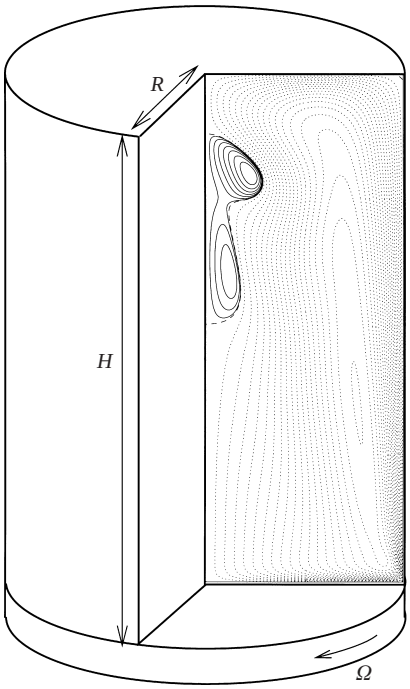

FIGURE 1. Schematic of the flow configuration with inset contours of streamfunction.

directions. This flow is then turned radially inwards by the top stationary endwall and swirls back down the axis. Hence the bottom endwall drives a swirling overturning flow. An interesting characteristic of these base flows is that for Re sufficiently large, regions of reversed axial flow can occur in the central vortex core; these features are known as vortex breakdowns. Vogel (1968) identified a steady vortex breakdown in his experiments, and Escudier (1984) experimentally mapped out the envelope of cylinder aspect ratios and flow Reynolds numbers within which vortex breakdowns – sometimes as many as three on an axial traverse – are observed.

Much of the past work on these enclosed swirling flows has the study of steady vortex breakdown behaviour as a central theme. In essence, those studies explored the features of the basic state, i.e. the steady axisymmetric flow. More recently, attention has turned to the stability of the basic state. Escudier's experiments showed that if the flow reaches a steady state, it is axisymmetric. Experimental and numerical studies have examined the flow topology of the basic states (Escudier 1984; Lugt & Abboud 1987; Lopez 1990). Studies of the onset of unsteadiness when the governing equations are restricted to an axisymmetric subspace have shown that the basic state loses stability via a supercritical Hopf bifurcation (Lopez & Perry 1992; Tsitverblit 1993; Sørensen & Christensen 1995; Gelfgat, Bar-Yoseph & Solan 1996). In both experimental and numerical investigations of the bifurcation behaviour, the cylinder aspect ratio is generally held fixed, and the Reynolds number is used as the bifurcation parameter.

It is clear that in this flow symmetries play an important dynamical role and a central issue that needs further attention is the question of symmetry breaking. The system, i.e. the governing equations and the boundary conditions, are invariant to arbitrary rotations about the axis, the $SO(2)$ symmetry, and arbitrary translations in

time. The implication for the basic state is that it too possesses these symmetries and so is steady and axisymmetric. The symmetries also determine how the basic state may lose stability (Iooss & Adelmeyer 1998; Chossat & Lauterbach 2000). Rotating waves and modulated rotating waves are generic features of flows with $SO(2)$ symmetry (see e.g. Rand 1982); however most studies on rotating waves in fluids have dealt with flows such as Taylor–Couette, where Reynolds number transitions to rotating waves (which appear steady in an appropriate rotating reference frame) precede other unsteady behaviour, such as axisymmetric modulation, and the bifurcation diagrams are further complicated by other symmetries related to reflections and/or translations in the axial direction. In the present case, unsteadiness first sets in as axisymmetric limit-cycle flows at Reynolds numbers below those for which $SO(2)$ symmetry is broken. Symmetry breaking then results directly in modulated rotating waves (without an intermediate pure rotating wave state), the modulation being axisymmetric in nature and strongly coupled to the underlying axisymmetric unsteadiness.

For cylindrical lid-driven cavities with aspect ratios in the range $1 < \Lambda < 4$, Hopf bifurcations are the only codimension-1 bifurcations that have been observed experimentally and numerically, and predicted from linear stability analysis. For this $SO(2)$-equivariant system, the Hopf bifurcation can have two types: either it breaks symmetry and the bifurcated state is a rotating wave (RW), or the symmetry is preserved beyond the bifurcation and the result is a time-periodic $SO(2)$-symmetric state. The linear stability analysis of Gelfgat, Bar-Yoseph & Solan (2001) considered general three-dimensional perturbations to the basic state. For low aspect ratios, $1 < \Lambda < 1.63$, their analysis predicts a symmetry-breaking Hopf bifurcation to a RW state with azimuthal wavenumber $k = 2$. This has recently been confirmed via three-dimensional direct numerical simulation (DNS) (Marques, Lopez & Shen 2002), where in addition the dynamics associated with the codimension-2 double Hopf bifurcation have been explored where the two types of Hopf bifurcation coincide near $\Lambda = 1.6$. For $\Lambda > 2.76$ the stability analysis again predicts a symmetry-breaking Hopf bifurcation to a RW with $k = 4$, and this has also been recently investigated via three-dimensional DNS (Marques & Lopez 2001). At intermediate aspect ratios ($1.63 < \Lambda < 2.76$) however, the predicted bifurcated state is axisymmetric. This is consistent with experiments (Escudier 1984; Stevens, Lopez & Cantwell 1999) and three-dimensional DNS (Blackburn & Lopez 2000). Thus the nature of the first instability of the basic state that presents itself with increasing Re is now clear. The subsequent instability phenomena of the unsteady flow regimes are largely unknown. In this range of intermediate aspect ratios, the $\Lambda = 2.5$ case is the most extensively studied, and we now briefly review what past investigations have revealed about it.

For $\Lambda = 2.5$ the flow is steady and axisymmetric for $Re \lesssim 2700$, with a double vortex breakdown; for comparisons of experimental dyelines and computed streamlines, see Lopez (1990) and Blackburn & Graham (2000). According to the analysis of Gelfgat *et al.* (2001), the system bifurcates to a time-periodic axisymmetric state at $Re \approx 2706$.

A recent experimental study (Stevens *et al.* 1999) identified three solution branches in the Reynolds number range 2700–4000. From analysis of the temporal behaviour of dye sheets near the axis of the cylinder, it was observed that each solution branch has an associated distinct dominant frequency. Flows of the first branch are axisymmetric and periodic from the onset of unsteadiness at $Re \approx 2700$, having associated non-dimensional period $\tau_1 = \Omega T_1 \approx 36$; the branch extends to $Re \approx 3500$. Flows of the second branch also produce periodic on-axis motion of the dye sheet, with $\tau_2 = \Omega T_2 \approx 28$, $Re > 3500$, but appear to be non-axisymmetric. A third branch, overlapping the other two for $3200 < Re < 3700$, has quasi-periodic flows that

also appear to be non-axisymmetric, with fundamental period $\tau_3 = \Omega T_3 \approx 57$, and with an additional very-low-frequency (VLF) modulation. In the same study, axisymmetric numerical simulations also produced three solution branches with associated fundamental periods of oscillation that were very similar to those observed experimentally.

Inspired by this ability to capture many of the temporal characteristics on the three experimentally observed branches with axisymmetric computations, Lopez, Marques & Sanchez (2001) studied the linear stability of the basic state to axisymmetric perturbations, considering not only the first bifurcation, to which linear stability studies are typically restricted, but also subsequent bifurcations of the basic state as Re is increased. As was expected, the first branch of periodic solutions observed by Stevens *et al.* (1999) corresponded to the first Hopf bifurcation mode of the basic state, which was predicted to occur at $Re \approx 2707$ (cf. 2706 predicted by Gelfgat *et al.* 2001). Lopez *et al.* were also able to identify the other periodic branch observed in the experiments with the third Hopf mode of the basic state. The branch with quasi-periodic solutions possessing a VLF modulation could not be conclusively linked to the Hopf modes of the basic state, but it was noted that the second and third Hopf modes bifurcated from the basic state at very proximate values of Re, suggesting that this VLF branch may possess mixed-mode solutions.

The computational studies for $\Lambda = 2.5$ outlined above were axisymmetric, whereas the experiments of Stevens *et al.* clearly demonstrated that flows on at least two of the three solution branches had broken axisymmetry. Neither the precise nature nor dynamics of this symmetry breaking received detailed study there.

In a brief Letter, Blackburn & Lopez (2000) made a first attempt at addressing these issues using three-dimensional DNS. This present paper is a full account of our subsequent investigation, in which a number of new results are established. We have determined that the solutions of the first branch that is observed to bifurcate from the basic state at $Re \approx 2700$ are stable to three-dimensional perturbations over the entire range of Re for which it exists (up to ≈ 3500), and the frequency of oscillation varies only very slightly with Re, staying close to the first Hopf frequency of the basic state. We refer to this branch of axisymmetric periodic solutions as branch A. The other branch which in the axisymmetric restriction has periodic solutions, and which exists for $Re \geqslant 3500$, has solutions that are unstable to three-dimensional perturbation. In fact, we have found two corresponding branches of three-dimensional solutions, one with azimuthal wavenumber 5 and the other with wavenumber 6. These two co-existing modulated rotating wave (MRW) states each have two incommensurate frequencies associated with them, one being the precession frequency of the azimuthal wave structure, and the other being the frequency for the underlying axisymmetric oscillation, which is very close to the third Hopf frequency of the basic state. These MRW states are referred to as M_5 and M_6 respectively; when restricted to an axisymmetric subspace, we refer to M_0 states; collectively this set is called the M solution branch. The quasi-periodic VLF-modulated solutions of the remaining branch are found here to be stable to three-dimensional perturbations over the middle range in Re for which it exists. However, the associated solutions are unstable to azimuthal wavenumber 5 at the high- and low-Re ranges of the branch, leading to MRW states with quasi-periodic modulation via Hopf-like bifurcations from the quasi-periodic axisymmetric state. These states are referred to as V_0 when axisymmetric and V_5 when possessing a MRW; collectively the V solution branch.

The balance of the paper is organized as follows: § 2 describes the computational technique used to solve the three-dimensional Navier–Stokes equations, along with

convergence tests. In § 3, details of computations restricted to an axisymmetric invariant subspace are presented and compared with previous experimental and computational results. Section 4 considers symmetry breaking of the results in § 3 and details the temporal and spatial characteristics of the resulting modulated rotating waves. Section 5 summarizes and discusses the results, and considers remaining open questions.

2. Computational methods

2.1. *Continuum evolution equations*

Our starting point is the incompressible Navier–Stokes equations

$$\partial_t \boldsymbol{u} + \boldsymbol{N}(\boldsymbol{u}) = -\frac{1}{\rho}\nabla p + \nu\nabla^2\boldsymbol{u}, \tag{2.1}$$

$$\nabla\cdot\boldsymbol{u} = 0, \tag{2.2}$$

where $\boldsymbol{u} = \boldsymbol{u}(z,r,\theta,t) = (u,v,w)(t)$ is the velocity field, and $\boldsymbol{N}(\boldsymbol{u})$ represents nonlinear advection terms. The variables z, r, θ and t are respectively the axial, radial, azimuthal and time coordinates and u, v, w the velocity components in the axial, radial and azimuthal directions. The nonlinear terms can be assembled in a variety of ways; we employ the 'skew-symmetric' form $\boldsymbol{N}(\boldsymbol{u}) = (\boldsymbol{u}\cdot\nabla\boldsymbol{u} + \nabla\cdot\boldsymbol{u}\boldsymbol{u})/2$.

As a consequence of rotation symmetry, the velocity must be 2π-periodic in θ and the velocity field can be projected exactly onto a set of two-dimensional complex Fourier modes $\hat{\boldsymbol{u}}_k$ by

$$\hat{\boldsymbol{u}}_k(z,r,t) = \frac{1}{2\pi}\int_0^{2\pi} \boldsymbol{u}(z,r,\theta,t)\exp(-\mathrm{i}k\theta)\,\mathrm{d}\theta \tag{2.3}$$

where k is an integer wavenumber. The velocity field has the associated Fourier series reconstruction

$$\boldsymbol{u}(z,r,\theta,t) = \sum_{k=-\infty}^{\infty} \hat{\boldsymbol{u}}_k(z,r,t)\exp(\mathrm{i}k\theta). \tag{2.4}$$

We introduce the following notation for the gradient and Laplacian of a (complex) scalar, as applied to mode k of a Fourier decomposition:

$$\nabla_k = \left(\partial_z, \partial_r, \frac{\mathrm{i}k}{r}\right), \quad \nabla_k^2 = \partial_z^2 + \frac{1}{r}\partial_r(r\partial_r) - \frac{k^2}{r^2} = \nabla_{rz}^2 - \frac{k^2}{r^2}. \tag{2.5}$$

The cylindrical components of the transformed momentum equations read

$$\partial_t\hat{u}_k + \widehat{\boldsymbol{N}(\boldsymbol{u})}_{zk} = -\frac{1}{\rho}\partial_z\hat{p}_k + \nu\left(\nabla_{rz}^2 - \frac{k^2}{r^2}\right)\hat{u}_k, \tag{2.6}$$

$$\partial_t\hat{v}_k + \widehat{\boldsymbol{N}(\boldsymbol{u})}_{rk} = -\frac{1}{\rho}\partial_r\hat{p}_k + \nu\left(\nabla_{rz}^2 - \frac{k^2+1}{r^2}\right)\hat{v}_k - \nu\frac{2\mathrm{i}k}{r^2}\hat{w}_k, \tag{2.7}$$

$$\partial_t\hat{w}_k + \widehat{\boldsymbol{N}(\boldsymbol{u})}_{\theta k} = -\frac{\mathrm{i}k}{\rho r}\hat{p}_k + \nu\left(\nabla_{rz}^2 - \frac{k^2+1}{r^2}\right)\hat{w}_k + \nu\frac{2\mathrm{i}k}{r^2}\hat{v}_k, \tag{2.8}$$

where $\widehat{\boldsymbol{N}(\boldsymbol{u})}_{zk}$ etc. represent mode-k components of the transformed nonlinear terms. The change of variables $\tilde{v}_k = \hat{v}_k + \mathrm{i}\hat{w}_k$, $\tilde{w}_k = \hat{v}_k - \mathrm{i}\hat{w}_k$ is introduced to decouple the

linear terms in the equations (Orszag 1974), giving

$$\partial_t \hat{u}_k + \widehat{\boldsymbol{N}(\boldsymbol{u})}_{zk} = -\frac{1}{\rho}\partial_z \hat{p}_k + \nu\left(\nabla^2_{rz} - \frac{k^2}{r^2}\right)\hat{u}_k, \tag{2.9}$$

$$\partial_t \tilde{v}_k + \widetilde{\boldsymbol{N}(\boldsymbol{u})}_{rk} = -\frac{1}{\rho}\left(\partial_r - \frac{k}{r}\right)\hat{p}_k + \nu\left(\nabla^2_{rz} - \frac{[k+1]^2}{r^2}\right)\tilde{v}_k, \tag{2.10}$$

$$\partial_t \tilde{w}_k + \widetilde{\boldsymbol{N}(\boldsymbol{u})}_{\theta k} = -\frac{1}{\rho}\left(\partial_r + \frac{k}{r}\right)\hat{p}_k + \nu\left(\nabla^2_{rz} - \frac{[k-1]^2}{r^2}\right)\tilde{w}_k, \tag{2.11}$$

where also $\widetilde{\boldsymbol{N}(\boldsymbol{u})}_{rk} = \widehat{\boldsymbol{N}(\boldsymbol{u})}_{rk} + \mathrm{i}\widehat{\boldsymbol{N}(\boldsymbol{u})}_{\theta k}$ and $\widetilde{\boldsymbol{N}(\boldsymbol{u})}_{\theta k} = \widehat{\boldsymbol{N}(\boldsymbol{u})}_{rk} - \mathrm{i}\widehat{\boldsymbol{N}(\boldsymbol{u})}_{\theta k}$.

2.2. *Boundary conditions*

The appropriate boundary conditions to be applied at the axis are derived from solvability requirements and kinematic constraints on scalar and velocity fields at the origin, as described by Batchelor & Gill (1962), Shen (1997) and Tomboulides & Orszag (2000). While, in principle, regularity conditions at the axis impose constraints on successively higher radial derivatives of modal variables with increasing mode number (Tuckerman 1969), in practice we only apply the essential boundary conditions needed to solve variational equations for modal pressures and velocities, augmented by a minimal subset of radial parity requirements (Lopez, Marques & Shen 2002), and the required smoothness is achieved asymptotically as spatial resolution is increased. These considerations lead to the following modal dependence of boundary conditions at the axis ($r = 0$):

$$\left.\begin{array}{ll} k = 0\text{:} & \partial_r \hat{u}_0 = \tilde{v}_0 = \tilde{w}_0 = \partial_r \hat{p}_0 = 0; \\ k = 1\text{:} & \hat{u}_1 = \tilde{v}_1 = \partial_r \tilde{w}_1 = \hat{p}_1 = 0; \\ k > 1\text{:} & \hat{u}_k = \tilde{v}_k = \tilde{w}_k = \hat{p}_k = 0. \end{array}\right\} \tag{2.12}$$

At solid or moving walls, the fluid velocities are set to match the prescribed wall velocities, and a boundary condition for the pressure can be derived by taking the dot product of the domain unit outward normal $\boldsymbol{n}$ with the momentum equations to produce

$$\partial_n \hat{p}_k = \rho \boldsymbol{n} \cdot (-\widehat{\boldsymbol{N}(\boldsymbol{u})}_k - \nu \nabla \times \nabla \times \hat{\boldsymbol{u}}_k - \partial_t \hat{\boldsymbol{u}}_k), \tag{2.13}$$

where the rotational form of the viscous term exploits the solenoidality of the velocity, and for the present application $\partial_t \boldsymbol{u} = 0$ at all solid boundaries.

2.3. *Discrete evolution equations*

For time evolution a mixed implicit–explicit time-split scheme based on backwards differentiation is employed (Karniadakis, Israeli & Orszag 1991); all the work presented here used a second-order-time variant of the method. The rotational form of the viscous term in (2.13) reduces splitting errors at prescribed-velocity boundaries to the same order as the time stepping.

The spatial discretization employs Fourier expansions in the azimuth and spectral elements in the meridional semiplane. The infinite set of Fourier modes (2.4) is truncated at some finite wavenumber N:

$$\boldsymbol{u}(z, r, \theta, t) = \sum_{k=-N}^{N-1} \hat{\boldsymbol{u}}_k(z, r, t)\exp(\mathrm{i}k\theta), \tag{2.14}$$

and as the modes possess the symmetry $\hat{\boldsymbol{u}}_{-k} = \hat{\boldsymbol{u}}_k^*$, in practice we need keep only the positive-wavenumber half of the spectrum ($k \geqslant 0$).

Spatial discretisation in the meridional (z, r)-semiplane employs spectral elements, with some similarities to the techniques used by Ghidersa & Dŭsek (2000) and Tomboulides & Orszag (2000). The approach we have adopted uses the standard Gauss–Lobatto–Legendre (GLL) basis for all elements, and sets singular terms equal to zero at the axis. As pointed out by Tomboulides & Orszag (2000), one type of fully consistent approach would employ, on elements that touch the axis, expansion functions with special Jacobi polynomials in the radial direction and use l'Hopital's rule to evaluate the $1/r$ and $1/r^2$ terms in (2.9)–(2.11). For modal variables other than $\hat{u}_0$, $\tilde{w}_1$ and $\hat{p}_0$, our method amounts to assuming that values go towards zero (as required by (2.12)) faster than r^2 as $r \to 0$. In practice, this method preserves spectral convergence for typical axisymmetric problems (Rønquist 1988; Gerritsma & Phillips 2000), and our experience is that while asymptotic convergence rates of third order may be observed for non-axisymmetric problems, initial convergence remains spectral. In addition, the method retains the numerical efficiency of standard spectral element approaches.

The planar/Fourier representation of three spatial dimensions leads naturally to parallel implementations in which for most of the time step each process carries a subset of two-dimensional complex modes. The nonlinear terms in the Navier–Stokes equations are formed pseudospectrally with the aid of interprocess memory exchanges. We have used this approach for most of our full DNS studies, but in the parallel implementation, nonlinear product terms are not dealiased in the azimuth. In order to assess the effect of aliasing we employed a non-parallel code variant that performs dealiasing in the azimuth using the 3/2 rule. This code variant was also used for all the computations restricted to an invariant subspace with P-fold symmetry in the azimuth (see § 2.5).

The spectral element outlines of the mesh used in the (z, r)-semiplane are shown in figure 2. The same 60-element layout was used for all testing and simulations. No special treatment, other than mesh refinement, is used to deal with the boundary condition discontinuity encountered at $(z/H = 0, r/R = 1)$, where the rotating endwall meets the stationary part of the cylinder.

2.4. *Convergence tests*

In order to demonstrate the spatial and temporal convergence of the simulation method, time series data extracted at $(z/H = 0.8, r/R = 0.7)$ have been analysed at varying GLL basis order, N_p, for a single Reynolds number, $Re = 4000$, near the upper extent of the range in Re investigated. These tests are for computations restricted to an axisymmetric subspace, as this is sufficient to test for grid independence in (z, r). At this Reynolds number, the flow is periodic, and experimental results and axisymmetric simulations presented in Stevens *et al.* (1999) both give the oscillation period as $\Omega T \simeq 28$. In table 1, we show the oscillation period and the minimum and maximum radial velocity at the point $(z/H = 0.8, r/R = 0.7)$ as a function of GLL polynomial order N_p at a fixed time step $\Omega\Delta t = 0.0125$. Results are converged to three significant figures or better with $N_\mathrm{p} \geqslant 7$. In table 2, we show the corresponding information at a fixed GLL polynomial order $N_\mathrm{p} = 9$ as a function of the time step $\Omega\Delta t$; over the range $0.005 < \Omega\Delta t < 0.015$ the results are almost invariant. All remaining results reported here are for a fixed GLL polynomial order $N_\mathrm{p} = 7$, and time steps $\Omega\Delta t$ in the range 0.0125–0.015.

N_p	N_{tot}	ΩT	$\min v/R\Omega$	$\max v/R\Omega$	mean $w/R\Omega$
4	1025	28.285	-4.6160×10^{-3}	3.2943×10^{-3}	97.562×10^{-3}
5	1581	28.260	-7.3226×10^{-3}	2.5324×10^{-3}	98.154×10^{-3}
6	2257	28.281	-7.1975×10^{-3}	2.6199×10^{-3}	98.180×10^{-3}
7	3053	28.282	-7.2067×10^{-3}	2.6349×10^{-3}	98.184×10^{-3}
8	3969	28.281	-7.1809×10^{-3}	2.6309×10^{-3}	98.189×10^{-3}
9	5005	28.281	-7.1827×10^{-3}	2.6332×10^{-3}	98.185×10^{-3}

TABLE 1. Results of spatial convergence tests for an axisymmetric simulation at $Re = 4000$ and $\Omega\Delta t = 0.0125$, showing period of oscillation ΩT, minimum and maximum radial velocities, and mean azimuthal velocity at ($z/H = 0.8$, $r/R = 0.7$) as a function of GLL polynomial order N_p (N_{tot} is the number of independent mesh points in the semiplane for each value of N_p).

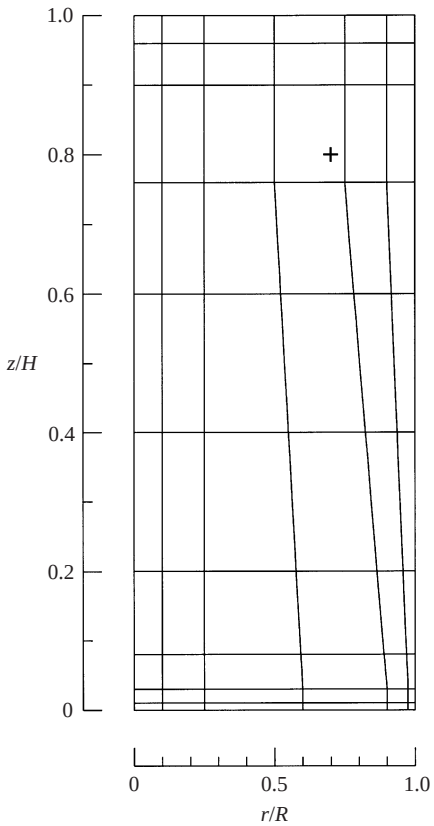

FIGURE 2. Spectral element mesh used to discretize the meridional semiplane. Cylinder axis to left, rotating endwall at bottom. The cross at ($z/H = 0.8$, $r/R = 0.7$) shows the location at which axisymmetric convergence test data are extracted.

2.5. *Three-dimensional computations*

As noted in § 2.1, the minimum required periodic module in the azimuth is $\theta = 2\pi$. The RW solutions that evolve with breakage of axisymmetry often retain more than the minimum degree of symmetry, typically a P-fold symmetry with $P = 5$ or 6 for the current problem (Blackburn & Lopez 2000). Such solutions are invariant to rotations about the axis by angles $2\pi n/P$, $n = 0, 1, \ldots, \infty$. Energies in modes

$\Omega\Delta t$	ΩT	$\min v/R\Omega$	$\max v/R\Omega$	mean $w/R\Omega$
0.015	28.281	-7.1828×10^{-3}	2.6332×10^{-3}	98.185×10^{-3}
0.0125	28.281	-7.1827×10^{-3}	2.6332×10^{-3}	98.185×10^{-3}
0.010	28.281	-7.1826×10^{-3}	2.6332×10^{-3}	98.185×10^{-3}
0.005	28.281	-7.1824×10^{-3}	2.6332×10^{-3}	98.185×10^{-3}

TABLE 2. Results of temporal convergence tests for an axisymmetric simulation at $Re = 4000$ and $N_p = 9$, showing period of oscillation ΩT, minimum and maximum radial velocities, and mean azimuthal velocity at ($z/H = 0.8$, $r/R = 0.7$) as a function of time step $\Omega\Delta t$.

that do not correspond to nP decay to machine noise levels in the absence of azimuthal aliasing. This allows considerable computational savings over a full three-dimensional computation retaining all Fourier modes up to N. By setting $k = nP$, we only integrate using the Fourier modes that do not decay to zero. We refer to this approach as computations restricted to an invariant subspace with P-fold symmetry. These subspaces are preserved by the Navier–Stokes equations.

Typically we have used all Fourier modes, up to a cut-off N, to establish the behaviour on each solution branch, checked the effect of azimuthal aliasing, then used the restriction to a subspace with P-fold symmetry to examine dynamical behaviour on each solution branch, backed up by spot-checks with all the Fourier modes to ensure that the branch is not unstable to other azimuthal modes. We have also performed spot-checks of azimuthal resolution, to check that sufficient harmonics have been used.

In addition, we have used completely axisymmetric simulations ($k = 0$, only) in order to establish behaviour in the axisymmetric subspace; this material is dealt with first, in § 3.

2.6. *Diagnostic information*

Evolution of the computed solutions is monitored through a variety of runtime diagnostics. Central to the current investigation is the (dimensionless) amount of flow kinetic energy contained in each Fourier mode k:

$$E_k = \frac{1}{2A\Omega^2R^2} \int_A \hat{\boldsymbol{u}}_k \cdot \hat{\boldsymbol{u}}_k^* \, r \, \mathrm{d}A, \tag{2.15}$$

where A is the area of the two-dimensional meridional semiplane and $\hat{\boldsymbol{u}}_k^*$ denotes the complex conjugate of the velocity data in the kth Fourier mode. The energy of the axisymmetric component of the flow is represented by E_0. As a consequence of Parseval's theorem, the (normalized) total kinetic energy of the solution integrated over the volume V is

$$E = \frac{1}{2V\Omega^2R^2} \int_V \boldsymbol{u} \cdot \boldsymbol{u} \, \mathrm{d}V = 2\pi \sum_{k=-N}^{N-1} E_k. \tag{2.16}$$

3. Dynamics restricted to an axisymmetric subspace

For $\Lambda = 2.5$ and $Re \in [2700, 4000]$, the solutions to the axisymmetric Navier–Stokes equations possess many of the temporal characteristics that are observed in physical experiments. As discussed in § 1, comparisons presented by Stevens *et al.* (1999) demonstrate this to be true even when the axisymmetric states are unstable to azimuthal modes. The close relationship between the behaviour of these axisymmetric

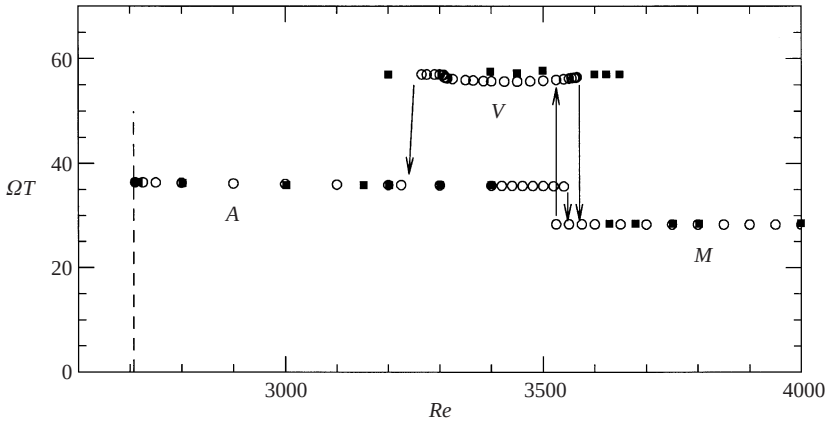

FIGURE 3. Fundamental oscillation periods for axisymmetric simulations (○), as a function of Reynolds number, with transitions between different solution branches indicated. Solutions on the V branch are quasi-periodic, with additional very-low-frequency modulations, while the A and M branches have periodic solutions. The dashed line at $Re = 2707$ indicates the Reynolds number for onset of unsteadiness at $\Lambda = 2.5$. Also shown are the experimentally measured values (■) obtained by Stevens *et al.* (1999).

states and that of the three-dimensional flows that occur is underlined by the fact that the axisymmetric mode typically retains more than 99% of the total flow kinetic energy (Blackburn & Lopez 2000). Thus, we begin the present study with a more detailed examination of the behaviour of axisymmetric flows in this parameter regime. In § 4 we will consider how these lose stability to azimuthal modes.

As outlined in § 1, for $\Lambda = 2.5$ the flow is steady and axisymmetric for $Re \lesssim 2700$. Stability analyses of Gelfgat *et al.* (2001) and Lopez *et al.* (2001) predict bifurcations to time-periodic axisymmetric states at $Re \approx 2706$ and 2707 respectively, and our present simulations place it in the Reynolds number range 2705–2710, as a supercritical Hopf bifurcation. The oscillatory behaviour appears as a periodic fluctuation of the vortex breakdown zone on the axis, a pulsation mode (Lopez & Perry 1992; Lopez *et al.* 2001). The characteristic period of the flow remains approximately constant near $\Omega T_1 \approx 36$ over the Reynolds number range for which it is observed, 2707–3500. For $Re \gtrsim 3500$, a second periodic branch is observed, with both the experimental and axisymmetric simulation results of Stevens *et al.* (1989) placing the fundamental period near $\Omega T_2 \approx 28$. In this case, the axisymmetric component of the oscillatory behaviour has the characteristic of a recirculation zone that periodically forms on the axis near the stationary wall and travels down the axis towards the rotating wall; a travelling mode. Overlapping these two branches in Reynolds number is a third solution branch; the experimental results of Stevens *et al.* (1999) give its extent as $3200 \lesssim Re \lesssim 3700$, with a characteristic fundamental frequency $\Omega T_3 \approx 57$. This branch has solutions characterized in addition by VLF modulations.

In figure 3 we present our computed fundamental periods of the axisymmetric solutions on the three branches for $Re \in [2710, 4000]$ (open circles). Beginning at $Re = 2710$ and extending to $Re \approx 3500$ is a branch on which solutions are time-periodic, with a characteristic period $\tau_1 = \Omega T_1 \approx 36$. This is the A branch. As Re is increased, there is a jump to a second periodic solution branch with $\tau_2 = \Omega T_2 \approx 28.3$ near $Re = 3500$, and this branch extends beyond $Re = 4000$. This is the M branch. Traversing to progressively lower Re on this branch, another jump occurs to a third solution branch where solutions are quasi-periodic, with a VLF modulation;

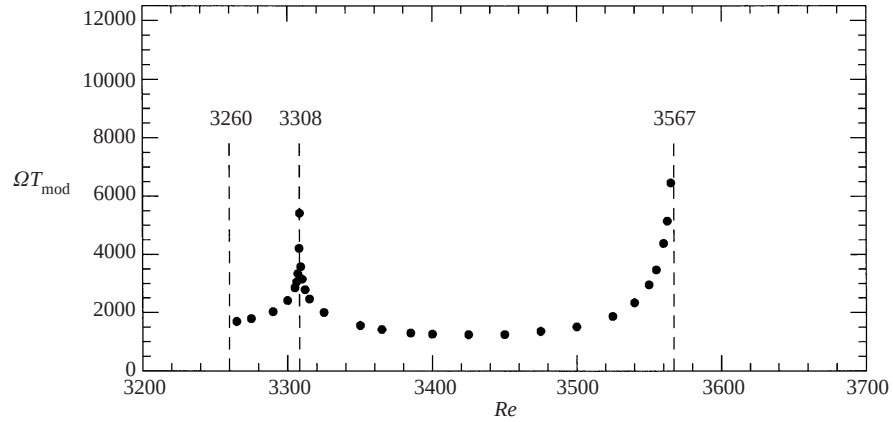

FIGURE 4. VLF modulation periods on the V solution branch for axisymmetric simulations, shown as a function of Reynolds number.

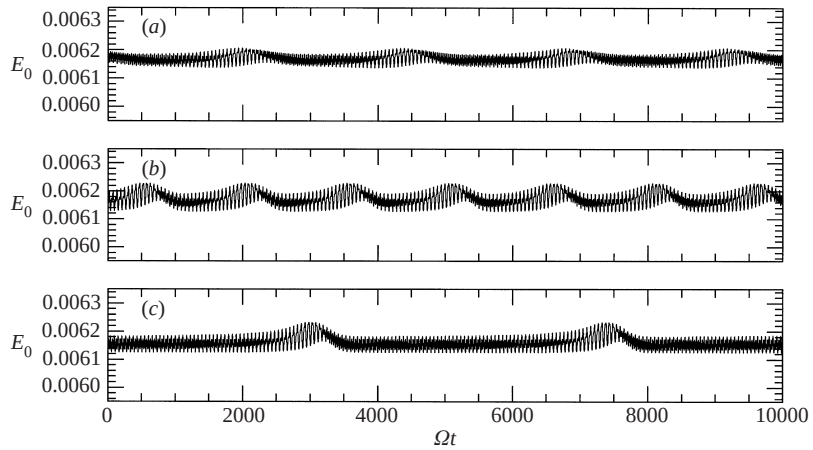

FIGURE 5. Time series of the energy, E_0, on the V_0 branch: (*a*) $Re = 3300$; (*b*) $Re = 3500$; (*c*) $Re = 3560$.

the V branch. Spectral analysis of solutions on this branch reveals, besides VLF, two dominant periods, one near $\tau_3 = \Omega T = 57$, the other near $\Omega T = 28$. Also included in the figure are the experimentally determined periods (filled squares) from Stevens *et al.* (1999), which are in very good agreement with the axisymmetric computations even though the flows on the M and V branches were both observed to be non-axisymmetric. Further, the VLF modulation on the V branch was also observed in the experiments (see figure 5*a*, Stevens *et al.* 1999. The associated long modulation periods, from the present axisymmetric calculations, are shown in figure 4. At the upper end of the Reynolds number range for the V axisymmetric branch, the modulation period appears to grow without bound as the jump to the M branch is approached. Another interesting feature of figure 4 is the cusp near $Re = 3308$, where again the modulation period becomes infinite.

Figure 5 shows time series of the energy, E_0, of the solutions on the modulated branch V at $Re = 3300$, 3500 and 3560. The long-period modulation is clearly seen in these – the behaviour is suggestive of a pair of weakly coupled oscillators near resonance.

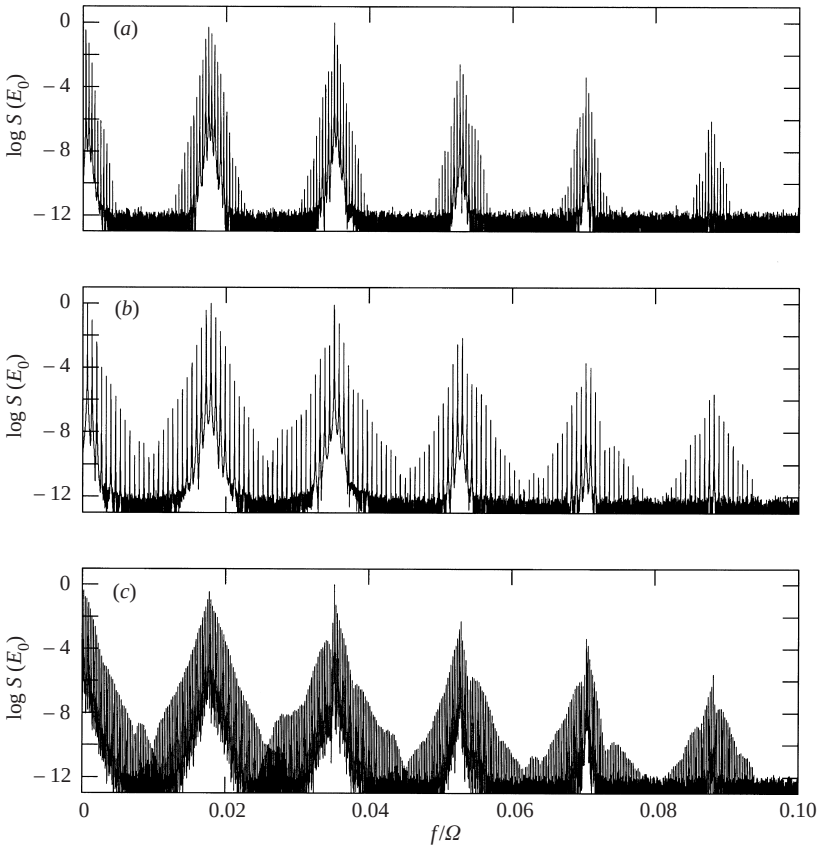

FIGURE 6. Spectra of the time series in figure 5: (*a*) $Re = 3300$; (*b*) $Re = 3500$; (*c*) $Re = 3560$. Spectral densities are given relative to peak values.

The power spectral densities of the time series of figure 5, $S(E_0)$, are shown in figure 6; the spectral resolution is $\Delta f/\Omega = 6.67 \times 10^{-6}$. All spectra consist of a main peak at $f_1/\Omega \approx 1.76 \times 10^{-2}$ (period ≈ 57) and another at $f_2/\Omega \approx 3.51 \times 10^{-2}$ (period ≈ 28), together with their harmonics. The main peaks are surrounded by a multitude of finely spaced and exponentially decaying sidebands, which result from the VLF modulation: the sideband spacing is the VLF, which also supplies the lowest-frequency spectral peak at f_{VLF}/Ω.

Examining the Reynolds numbers for the three spectra (3300, 3500 and 3560) we see that the first lies on the low-Reynolds-number side of the T_{mod} cusp seen in figure 4, the second and third above it. Detailed analysis of the spectral peak frequencies leads to the conclusion that for $Re = 3500$ and 3560, $f_{\mathrm{VLF}} = 2f_1 - f_2$, while for $Re = 3300$, $2f_1 - f_2 = 0$ to within the spectral resolution. In figure 7, $f_{\mathrm{VLF}} - (2f_1 - f_2)/\Omega$ and f_1/f_2 are plotted over the entire Re extent of the V branch. To the left of the cusp at $Re \approx 3308$ (see figure 4), $2f_1 = f_2$ but f_{VLF} is independent and varies with Re, while to the right of the cusp $f_{\mathrm{VLF}} = 2f_1 - f_2$ (i.e. f_{VLF} is a frequency of beating between $2f_1$ and f_2), and f_1/f_2 varies with Re. The implication is that only two of the three frequencies are ever independent, and the flows on the V branch correspond to 2-tori orbits when restricted to an axisymmetric subspace. The upper-Re limit of the V_0 solution branch occurs when f_1 becomes a subharmonic of f_2, which corresponds to the frequency for the M_0 branch, and at this point these branches join.

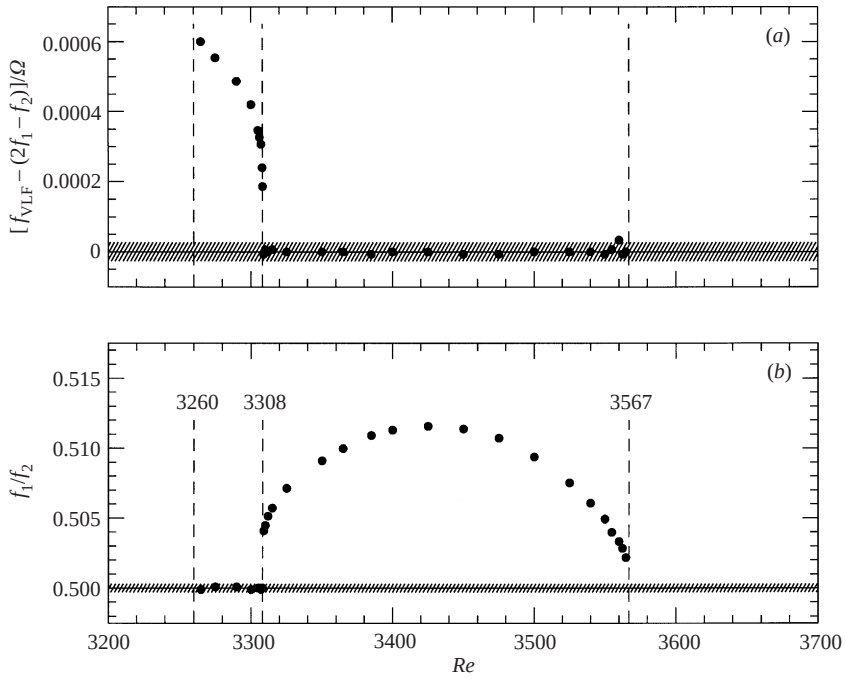

FIGURE 7. Variation of (*a*) $f_{\mathrm{VLF}} - (2f_1 - f_2)/\Omega$ and (*b*) f_1/f_2 with Re for the V_0 branch. Shaded bands indicate the level of uncertainty associated with spectral resolution.

As outlined in § 1, the work of Lopez *et al.* (2001) provides clear evidence that the A and M solution branches are associated with the first and third Hopf modes to bifurcate from the basic state above $Re = 2700$. Our conjecture is that the genesis of the V branch is as a mixed-mode between pairs of the first three Hopf modes.

4. Symmetry breaking to modulated rotating waves

The stability of the three solution branches obtained with axisymmetric simulations to non-axisymmetric perturbations was examined by lifting the axisymmetric solution onto a three-dimensional representation with $P = 1$ (i.e. with the minimum required symmetry: 2π-periodic in θ), perturbing the velocity field by the addition of Gaussian noise in the first Fourier mode, and evolving the system to a near-asymptotic state. The initial perturbation is distributed rapidly via convolution to drive all modes, after which the solution may evolve to select an unstable mode. The standard deviation of the initial perturbation was typically $1 \times 10^{-12} R\Omega$, although a level of $1 \times 10^{-8} R\Omega$ has also been used. The outcomes on each of the three solution branches have been checked using 32, 40 and 64 Fourier modes.

The evolution of a solution on the M branch at $Re = 4000$ is illustrated in figure 8. Soon after initiation, the $k = 5$ mode starts to gain energy, growing exponentially with time until it saturates at $\Omega t \approx 3000$. As the asymptotic state is approached, the $k = 5$ mode is the dominant non-axisymmetric mode, followed by its harmonics at $k = 10$, 15, etc. (i.e. $k = 5n$). Energies in other modes eventually decay to machine noise levels, in the absence of azimuthal aliasing (Blackburn & Lopez 2000), i.e. the solution evolves to an invariant subspace with a 5-fold azimuthal symmetry. The energy in the axisymmetric component of the flow, and its temporal behaviour, remain nearly unchanged by the transition to three-dimensionality. This is illustrated in figure 9 –

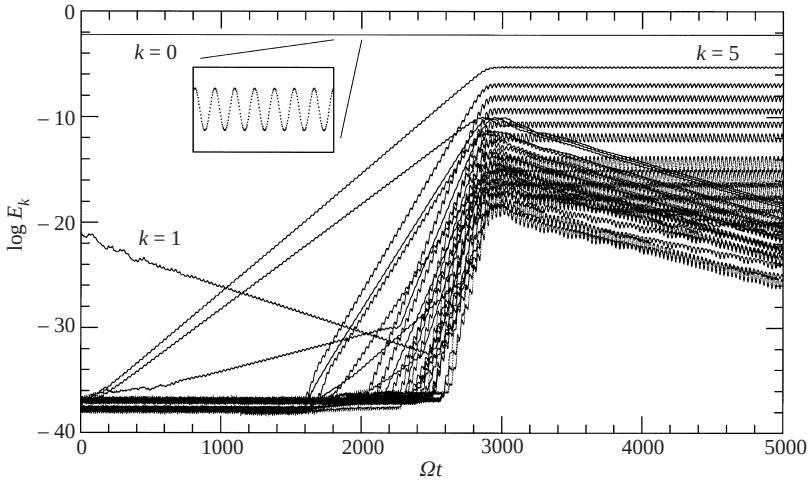

FIGURE 8. Growth of three-dimensional MRW instability on the M branch at $Re = 4000$, starting from an axisymmetric solution perturbed in the $k = 1$ Fourier mode. At the end of the integration period, the $k = 5$ mode and its harmonics are the dominant non-axisymmetric modes. The inset shows the temporal modulation of the $k = 0$ mode (ordinate scale greatly magnified).

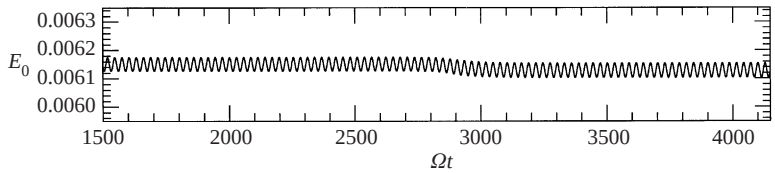

FIGURE 9. The small variation of energy in the axisymmetric mode during the transition shown in figure 8.

during transition the energy falls by less than 0.5% and the oscillation period rises slightly, to $\Omega T = 28.50$ (cf. table 2).

Similar perturbations were carried out at various Reynolds numbers on each of the A, M and V branches. The A branch was found to retain axisymmetry at all Reynolds numbers investigated (up to $Re = 3400$); after perturbation in the $k = 1$ mode, the energy in all modes $k \neq 0$ eventually decayed towards machine zero. On the V branch, only solutions with $P = 5$ azimuthal structure were observed; attempts to drive the solution by initializing with different modal states returned, after some time, to a $P = 5$ MRW. On the M branch, solutions with either $P = 5$ or $P = 6$ were observed, the choice being dependent on initial conditions. Once either state had been achieved, these solutions were stable to small perturbations (order $1 \times 10^{-12} R\Omega$) in the alternative leading mode.

In what follows, numeric subscripts are used to label the azimuthal periodicity of the asymptotic state under discussion, according to the leading non-axisymmetric mode; thus the non-axisymmetric solutions on the V branch correspond to V_5, while on the M branch we have observed both M_5 and M_6. We also use V_0 and M_0 to denote the corresponding axisymmetric states. The characteristics of example solutions on each of the A, M and V branches are described in § 4.1, followed by examination of the dynamical behaviour on the M branch (§ 4.2) and the V branch (§ 4.3).

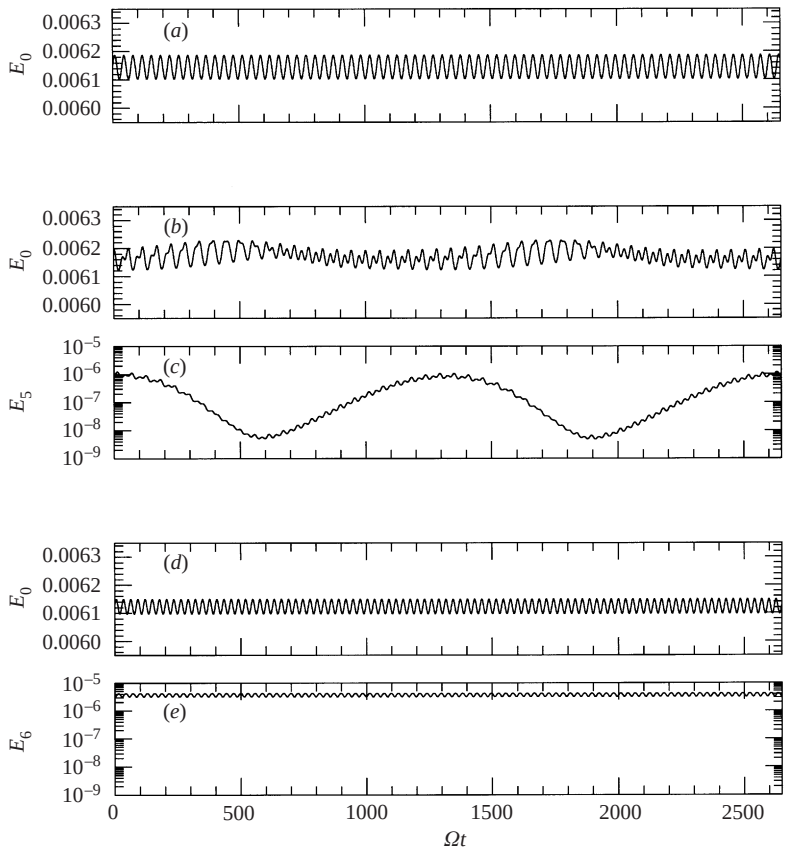

FIGURE 10. Time series of modal kinetic energies for the axisymmetric mode (E_0) and, if appropriate, for the leading non-axisymmetric mode at (*a*) $Re = 3000$, A branch; (*b*, *c*) $Re = 3500$, V_5 branch; (*d*, *e*) $Re = 4000$, M_6 branch.

4.1. *Three specimen solutions*

The three specimen solutions examined here correspond to Reynolds numbers of 3000, 3500 and 4000, producing asymptotic results on the A, V_5 and M_6 branches, respectively.

Figure 10 shows the time series of kinetic energy in the axisymmetric mode, and in the leading non-axisymmetric mode, if appropriate. The time interval represented, $\Omega t = 2650$, is sufficient to encompass two VLF modulation cycles of the V_5 solution at $Re = 3500$. The time series of E_0 are virtually indistinguishable, both in magnitude and frequency content, from their counterparts obtained with axisymmetric computations, described in § 3. The energies in the leading non-axisymmetric modes are at least two orders-of-magnitude smaller than those in the axisymmetric modes. Note also the approximate two orders-of-magnitude variation in E_5 over a VLF modulation cycle for the V_5 branch. The energies in the respective harmonics decay exponentially. The decay rates of the non-axisymmetric modes are approximated by $\mathrm{d}(\log\langle E_k\rangle)/\mathrm{d}k = -0.4$ for the V_5 solution and $\mathrm{d}(\log\langle E_k\rangle)/\mathrm{d}k = -0.25$ for the M_6 solution.

The spatial structures of the rotating waves are illustrated in figure 11, which shows isosurfaces of the azimuthal velocity and its perturbation for the V_5 and M_6 solutions. The V_5 solution is represented near a time where E_5 is maximum. The 5- and 6-fold azimuthal symmetry of the MRWs are clearly evident in the isosurfaces.

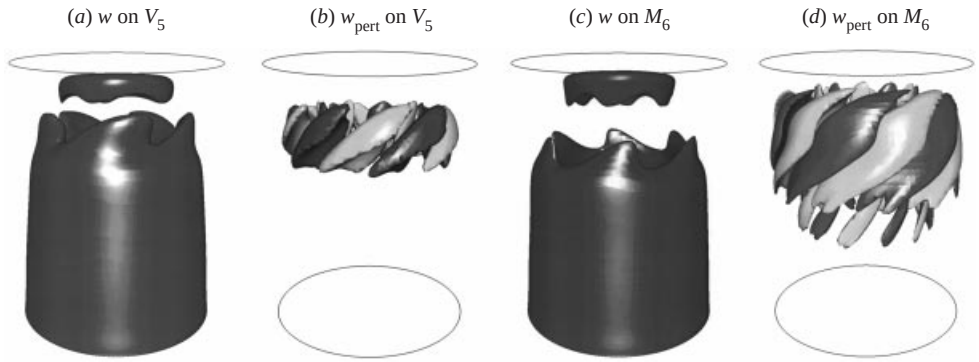

FIGURE 11. Perspective views of the rotating modulated waves of (a, b) the V_5 solution at $Re = 3500$ and (c, d) the M_6 solution at $Re = 4000$, showing isosurfaces of the azimuthal velocity component w and its perturbation w_{pert} (i.e. w minus the $k = 0$ contribution). The spinning endwall is at the bottom and rotates clockwise when viewed from above.

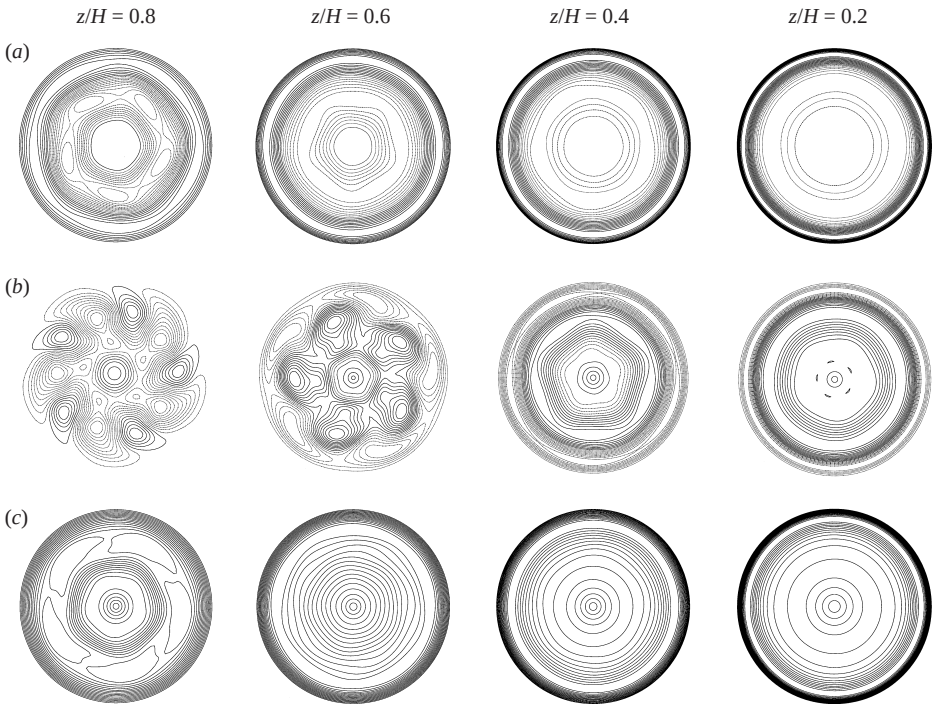

FIGURE 12. Contours of the instantaneous (*a*) axial, u, (*b*) radial, v, and (*c*) azimuthal, w, components of velocity at heights z/H as indicated, for the V_5 solution at $Re = 3500$. As observed looking from the stationary to spinning cylinder endwall.

These plots also suggest that the departure from axisymmetry is greatest towards the top stationary endwall.

Figures 12 and 13 show contours in (r, θ) of the three velocity components at various heights for the two solutions shown in figure 11. These further show that the azimuthal waves are concentrated near where the average azimuthal velocity is greatest ($r/R \approx 0.67$, $z/H \approx 0.8$) and that the flow near the axis remains nearly

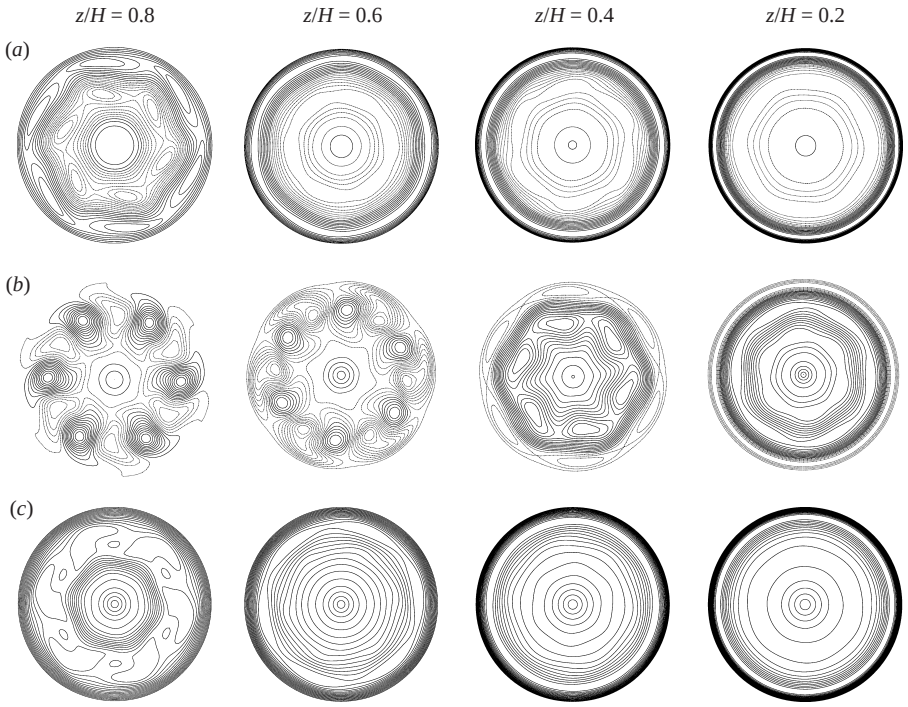

FIGURE 13. Contours of the instantaneous (*a*) axial, u, (*b*) radial, v, and (*c*) azimuthal, w, components of velocity at heights z/H as indicated, for the M_6 solution at $Re = 4000$.

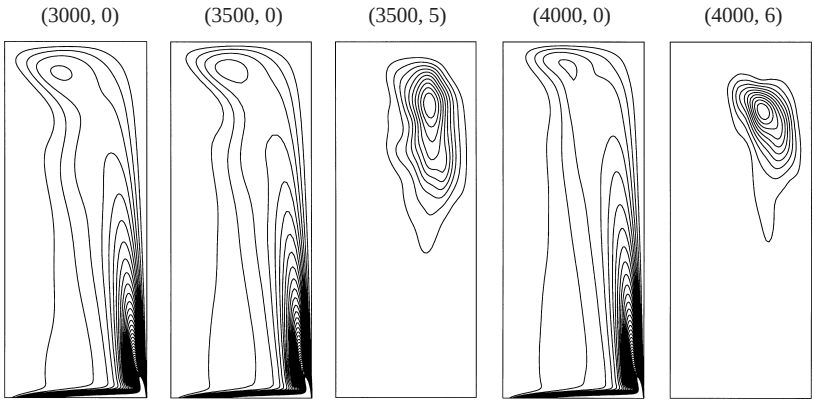

FIGURE 14. Contours of averaged flow kinetic energy $\langle \hat{\boldsymbol{u}}_k \cdot \hat{\boldsymbol{u}}_k^* \rangle / 2R^2\Omega^2$ in the meridional semi-plane for (Re, k) as indicated. In each plot the cylinder axis is to the left and the rotating endwall is at the bottom.

axisymmetric. Note again the very regular P-fold azimuthal structure; the modulation of the rotating waves is induced by the underlying axisymmetric behaviour.

The contour plots of time-averaged kinetic energy in the axisymmetric mode and the leading non-axisymmetric mode for the A, V and M solutions shown in figure 14 further illustrate the point that for the V_5 and M_6 solutions, the departure from axisymmetry is greatest near $z/H = 0.8$, $r/R = 0.67$, well away from the axis. The kinetic energy of the symmetry-breaking modes is concentrated near the tip of an

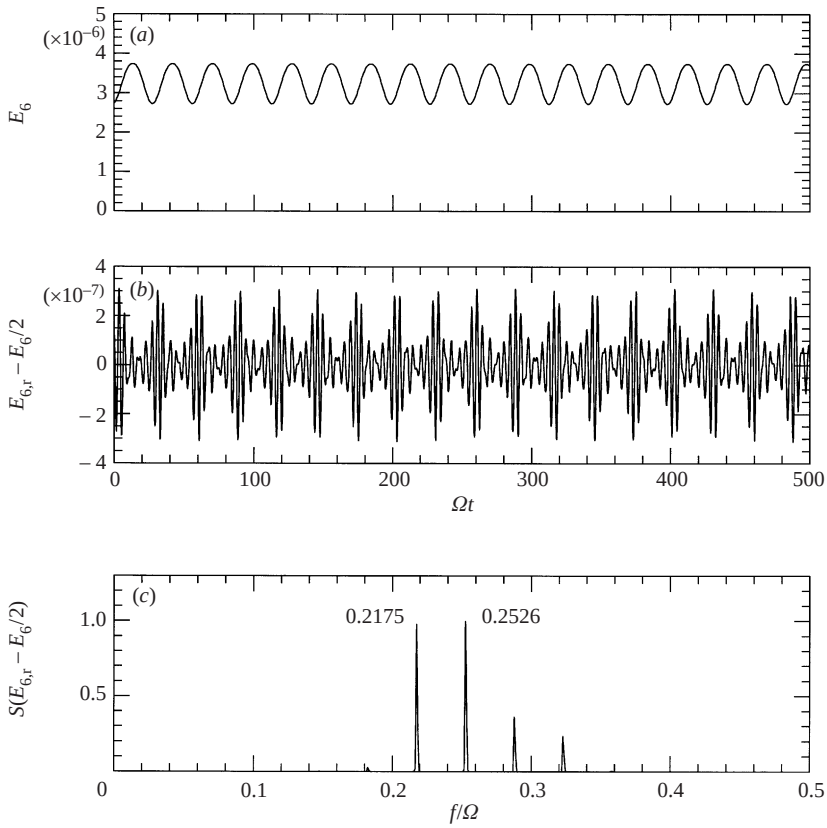

FIGURE 15. Frequency analysis for MRW precession rate of the M_6 solution at $Re = 4000$.

azimuthal wall jet that originates where the rotating endwall meets the stationary sidewall – this feature can be clearly identified in the $k = 0$ contours.

The azimuthal wave structures are modulated in time by the underlying axisymmetric behaviour of the flow. In addition, they possess another characteristic period, that associated with the rotation speed of the waves. Computation of this speed is complicated by the axisymmetric temporal modulation. A straightforward, but approximate, method is to view animations of isosurfaces such as those shown in figure 11, and count the frames required for one wave rotation. When using this method, it is readily apparent that the waves precess with the same sense as the endwall rotation (prograde precession). The observed precession speeds are close to those which correspond to the mean azimuthal flow velocities ($\langle w_p \rangle$) at locations where the mean non-axisymmetric energies reach maxima (z_p, r_p) in figure 14, producing $\Omega T = 2\pi\Omega r_p^2/R^2\langle w_p \rangle = 44.2$ for both the V_5 and M_6 states.

A more precise method to estimate precession speeds can be based in Fourier analysis of modal energies. Steps in the process are illustrated in figure 15. In figure 15(a), the time series of energy in the $k = 6$ Fourier mode (E_6) for the M_6 solution at $Re = 4000$ is shown; the characteristic period for the solution is $\Omega T = 28.50$, which derives from the axisymmetric fluctuation of energy. This time series does not reveal information about the rotating wave speed, just fluctuations in the total energy of the leading non-axisymmetric mode. The precession of the wave

corresponds to an oscillatory exchange of energy between the real (r) and imaginary (i) components of the Fourier mode, where $E_6 = E_{6,\mathrm{r}} + E_{6,\mathrm{i}}$.

Figure 15(b) shows time series of the component of energy that lies in the real part of the $k = 6$ mode, $E_{6,\mathrm{r}}$, with half the total energy, $E_6/2$, subtracted from it. The outcome resembles a high-frequency signal (caused by the precession) modulated by a lower-frequency one (the axisymmetric component, $\Omega T = 28.50$). Since the high-frequency signal derives from squared quantities (like u_{r}^2), we expect that the corresponding fluctuation in the modal data oscillates with half that frequency. The power spectrum of the time series of figure 15(b) is shown in figure 15(c). The main peak, at $f_o/\Omega = 0.2526$, corresponds to the high frequency evident in (b), and the spacing of the sidebands to $1/(28.5\Omega) = 0.03509$. Thus the real and imaginary components of the modal data oscillate at $f/\Omega = 0.2526/2 = 0.1263$, and the time taken for the wave to travel an angular displacement of $2\pi/6$ is $\Omega t = \Omega/f = 7.918$. The period for a full revolution is $\Omega T = 6 \times 7.918 = 47.50$, giving a precession rate $\omega/\Omega = 0.1322$.

The analysis for precession speed at $Re = 3500$ is similar but the time series and spectral density plots have additional detail as a consequence of the additional VLF modulation. The outcome of the analysis is a total precession period for the $P = 5$ MRW of $\Omega T = 47.69$, giving $\omega/\Omega = 0.1318$.

4.2. *Characteristics of the M solution branch*

Two asymptotic solutions evolved at $Re = 4000$, one with the leading non-axisymmetric mode $k = 5$, the other with $k = 6$, the outcome being dependent on the initial conditions. The behaviours were checked using both 32 and 64 Fourier modes in the azimuth, and the results were nearly identical. It appears then that there are at least two M solution branches: the investigation here is confined to the M_5 and M_6 cases.

Following the establishment of M_5 and M_6 states at $Re = 4000$, branch tracking was carried out using the three-dimensional code restricted to invariant subspaces with 5-fold and 6-fold azimuthal symmetry (see § 2.5), using eight Fourier modes, equivalent to employing 40 and 48 modes respectively in an unrestricted code. For both branches, the period of fluctuation of energy in the axisymmetric component of the flow remained very close to $\tau_2 = 28.50$. The upper Reynolds number limit of the branch tracking carried out was $Re = 4300$ – while the branches appear to continue to be stable at these and higher Reynolds numbers, this has not been established using the unrestricted code. The lower limits of Reynolds number for both branches lies a little below $Re = 3600$: for lower Reynolds numbers, solutions jump to the V_5 VLF-MRW branch. This conclusion has been checked with the unrestricted code, and is also very similar to the behaviour observed with axisymmetric simulations (see figure 3). When M_6 solutions jump to the V branch, $P = 6$ MRWs die and are replaced by $P = 5$ MRWs.

The M states (branches M_0, M_5 and M_6) are observable (i.e. M_0 is linearly stable in an axisymmetric subspace, and M_5 and M_6 are linearly stable to small three-dimensional perturbations) at $Re \approx 3600$, their amplitudes (E_0, E_5 and E_6) are all non-zero and all frequencies associated with these are finite. We are unable to definitively distinguish between the various possible bifurcation scenarios that lead to a stable M branch. The advent of numerical continuation techniques for limit cycles and 2-tori would assist in identifying the correct scenario.

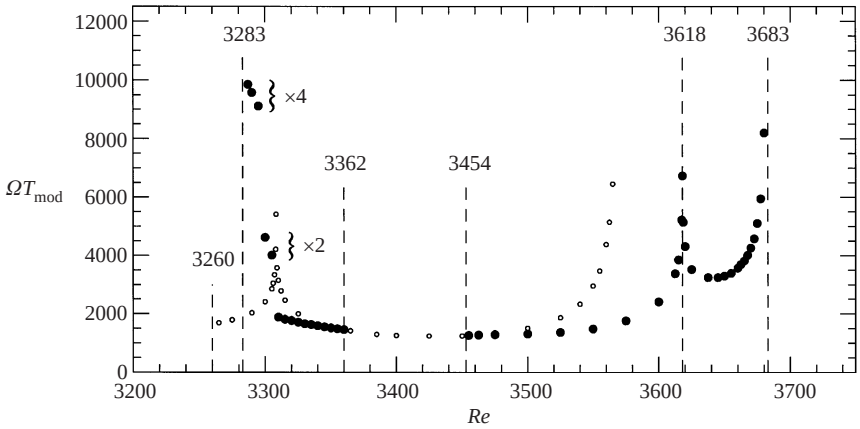

FIGURE 16. VLF modulation periods on the V branch. •, V_5; ○, V_0 (reproduced from figure 4). Note period-doubled and quadrupled values near $Re = 3300$.

4.3. *The V solution branch*

The behaviour on the V solution branch, by comparison with that on the M branch, is more complex, and there are more significant differences between the axisymmetric and non-axisymmetric behaviours. Owing to the VLF modulation, much longer integration times are required to obtain asymptotic results on the V branch than on the M branches, hence our branch-tracking computations are restricted to an invariant subspace with 5-fold azimuthal symmetry. We have employed four Fourier modes (corresponding to an equivalent 20 modes in an unrestricted code), as opposed to the eight used for the investigation of § 4.2. Quantitatively and qualitatively similar results for the whole of the V branch have also been obtained with two-mode computations (using wavenumbers 0 and 5), and for spot checks with unrestricted computations employing 32 modes and above.

All the time series results for the V branches have features comparable to those shown in figures 5 and 6: a VLF modulation, then two distinct, slightly incommensurate frequencies, $f_1/\Omega \approx 1/57$ and $f_2/\Omega \approx 1/28$. For the V_5 solutions, the energy in the non-axisymmetric modes has very similar frequency content to the axisymmetric mode, but shows very substantial amplitude variations during a VLF modulation cycle (figure 10*c*). Again owing to the combined expense of three-dimensional computations and the extremely long integration times required, we have not here carried through the kind of detailed frequency analysis that was used to produce figures 6 and 7 in § 3.

The VLF modulation periods for the V_5 branch are shown in figure 16, where they are compared with the V_0 results, reproduced from figure 4. The V_0 branch loses axisymmetry to a $P = 5$ MRW over two Reynolds number ranges: 3282–3362 and 3454–3683. It is seen that V_5 can be continued to higher Re than V_0 (3683 cf. 3567). The VLF period approaches infinity at two Reynolds numbers on the upper V_5 branch: near $Re = 3618$, and at the end of the branch, near $Re = 3683$. As Reynolds numbers were increased past 3683, the flow solution lost modulation and evolved to the M_5 branch. On the lower-Re V_5 branch, it can be seen that the cusp present near $Re = 3308$ on the V_0 branch disappears. At approximately the same Reynolds number on the V_5 branch, the VLF modulation undergoes a period doubling as Reynolds number is decreased, resulting in modulation periods

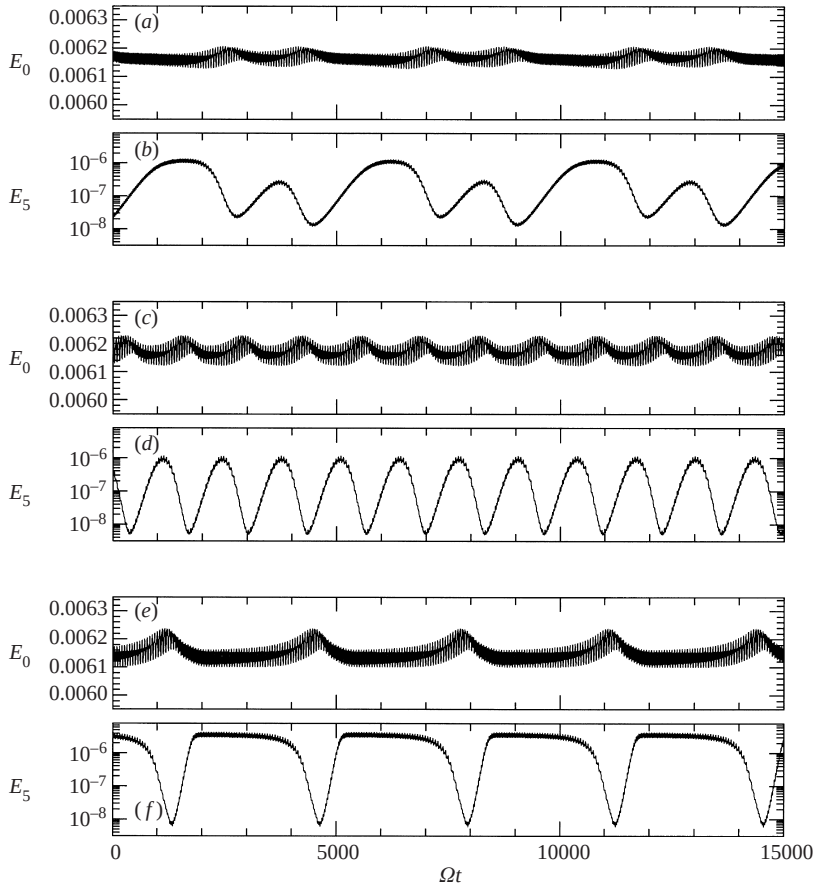

FIGURE 17. Time series of energies in the axisymmetric mode and the leading non-axisymmetric mode on the V_5 branch: (a,b) $Re = 3300$ – note period doubling; (b,c) $Re = 3500$; (e,f) $Re = 3650$.

$\Omega T_{\mathrm{mod}} \approx 4500$. As Reynolds numbers decrease further, another period doubling occurs ($\Omega T_{\mathrm{mod}} \approx 9000$), and finally, near $Re = 3283$, energies in non-axisymmetric modes die and the solution regains axisymmetry, with modulation periods returning to those of the V_0 branch.

Time series that illustrate the VLF modulation behaviour for the V_5 branch are presented in figure 17, which shows energy in the axisymmetric component of the flow, E_0, and the leading non-axisymmetric mode, E_5, for $Re = 3300$, 3500 and 3650. The period-doubling of the VLF modulation can be seen for the $Re = 3300$ case (figure 17a,b). The values for $Re = 3500$ (c,d) constitute an extended-time presentation of those in figure 10(b,c), while those in (e,f) are for $Re = 3650$, located between the two upper-Re cusps in figure 16. For all three cases, the energy in the leading non-axisymmetric mode is greatest when the axisymmetric component is lowest. Typically this occurs at times when the $\Omega T \approx 28$ behaviour appears to dominate the axisymmetric component. This again supports the idea that this branch is produced by mixed-mode behaviour – two modes are present, but only one supports symmetry-breaking RWs. The presence of the period-doubled behaviour does not result from the restriction to a subspace with 5-fold symmetry; the same behaviour

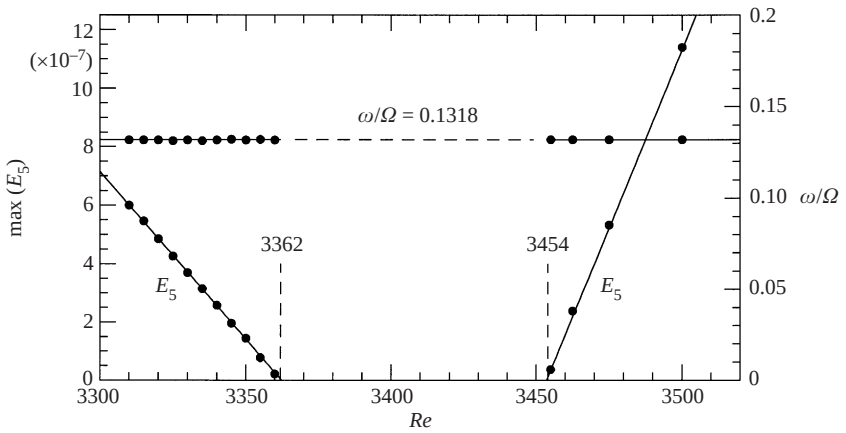

FIGURE 18. Peak energy in the leading non-axisymmetric mode, E_5, and MRW precession speed, ω/Ω, for the supercritical symmetry-breaking Hopf-type bifurcations on the V solution branch.

is observed in unrestricted computations, and is stable to small perturbations in non-leading modes.

As $Re \to 3362^-$ and $Re \to 3454^+$, modulation periods on the lower and upper V_5 segments asymptote to those for the V_0 branch. In figure 18 we show the peak energies in the $k = 5$ mode, $\max(E_5)$, and the MRW precession speeds near these two bifurcations from axisymmetry. In both cases $\max(E_5)$ rises linearly with changes in Reynolds number. The linear relationships indicate that the amplitude of the MRW varies with $|Re - Re_c|^{1/2}$, identifying these bifurcations from the quasi-periodic axisymmetric V_0 state as being of supercritical Hopf type. The MRW precession speeds stay constant at $\omega/\Omega = 0.1318$ for each bifurcation. As these are $SO(2)$ equivariant bifurcations, it is expected that the RW speeds have the form $\omega/\Omega = C_1 - C_2|Re - Re_c|$ (Knobloch 1994); here $C_2 \approx 0$ and $C_1 = 0.1318$ for each case, presumably owing to a high degree of similarity between the V_0 states from which each V_5 MRW bifurcates at $Re = 3362$ and 3454. Note that to three significant figures the phase speeds of RWs on the V and M branches are the same at $\omega/\Omega = 0.132$.

The maximum energy in the fifth azimuthal mode for the V_5 branch is shown as a function of Reynolds number in figure 19. Representations of Reynolds numbers for the V_0 branch are included, to emphasize the fact that the total range for the V branch predicted by our study is 3260–3683. Peak energies in the leading non-axisymmetric modes for the M_5 and M_6 branches are also presented; it is interesting that the peak energies for the V_5 and M_5 branches are nearly identical where they overlap in Reynolds number. This, in conjunction with figure 17(*e*,*f*) suggests that M_5 is one of the modes participating in a V_5 mixed-mode solution. The good match between the peak energies of the V_5 and M_5 solutions over a range of Reynolds numbers ($3580 < Re < 3683$) suggests the possibility that a V_6 solution branch might exist as well; however we have been unable to obtain one, even with selectively perturbed initial conditions, suggesting that if it does exist it is unstable. The ranges for the experimental observations in Stevens *et al.* (1999) are also presented in figure 19 (see figure 3 for point values). Overall, the agreement in extents of branches is good, and the slight overlap in the Re range for the V and M branches found in the experiments is also present in the computations. Note that the overlap region obtained from the three-dimensional computations is in much better quantitative agreement with the experiments than are the axisymmetric computations.

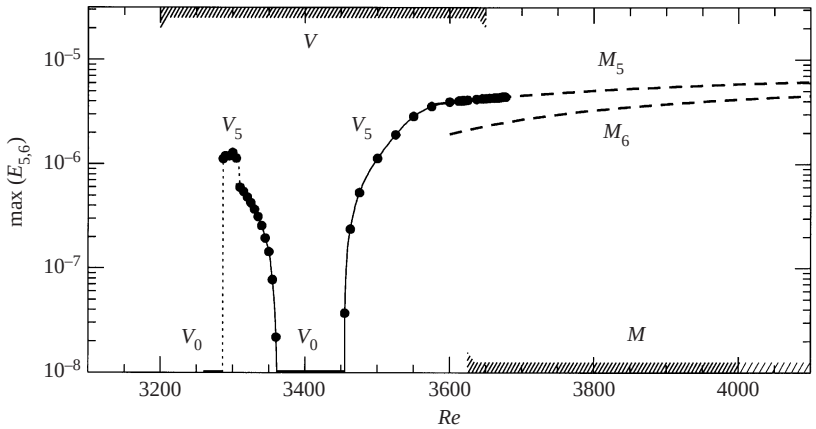

FIGURE 19. Peak value of energy in leading non-axisymmetric mode, max(E_5), on the V_5 branch, with corresponding values for the M_5 and M_6 branches indicated by dashed lines. The experimental observations of branch extents from Stevens *et al.* (1999) are also shown, hatched.

5. Discussion and conclusions

It is apparent from the work presented here that this very simple flow, which has just two governing parameters, Λ and Re, and two symmetries, invariance to time translations and fixed rotations about an axis, possesses a rich dynamic. As there are two control parameters, both codimension-1 and codimension-2 bifurcations are accessible in the system; by varying a single parameter (Re), we observe a codimension-1 projection of possible bifurcations.

Gelfgat *et al.* (2001) have recently analysed the first bifurcations from the steady, axisymmetric basic state for this flow, and in this paper we have examined in some detail a small portion of the regime where secondary bifurcations lead to multiple states, some of which are stable and co-exist. We have drawn on recent computational and experimental results to help fill in the picture, but even with the use of linear stability analysis, experiment and evolution of the three-dimensional Navier–Stokes equations, we are left with open questions. Some of these can potentially be resolved with the use of available numerical techniques, such as Floquet analysis. Comprehensive bifurcation analysis in the style of Mamun & Tuckerman (1995) will require development of efficient and robust analytical tools to enable continuation of unstable limit cycles and 2-tori. In addition, treatment of global phenomena associated with possible 1 : 2 resonant double Hopf bifurcations are yet to receive the detailed theoretical treatment necessary for unambiguous identification of such behaviour (Kuznetsov 1998).

We have established that for $\Lambda = 2.5$ and in the Reynolds number range above 2707, where the flow changes from axisymmetric and steady to axisymmetric and periodic via a supercritical Hopf bifurcation, up to $Re = 4300$, the upper limit of our work, three branches of stable orbits can be observed, and each possesses a characteristic temporal behaviour by which it can be readily identified. Limit cycle flows of the A branch remain periodic and axisymmetric over the range that they can be followed numerically and experimentally, $2707 < Re \lesssim 3500$, and have a characteristic period close to $\tau_1 = \Omega T = 36$ for this entire range. Flows of the M branch, which is stable for Reynolds number greater than approximately 3580, have a characteristic underlying period $\tau_3 = \Omega T = 28.5$, and are unstable to azimuthal

perturbations with either $P = 5$ or $P = 6$ wavenumbers. These rotating waves are modulated by the underlying axisymmetric behaviour, and have a prograde precession with angular speed $\omega/\Omega = 0.132$. The energy of the MRWs is concentrated in a region remote from the axis, and closer to the stationary endwall. The M branch is the third branch to bifurcate from the basic state as Re is increased with fixed $\Lambda = 2.5$: this is clear from the related work of Lopez *et al.* (2001). Floquet techniques may be used to study the stability of the M_0 branch to rotating waves, but these can only currently be employed where the axisymmetric state is stable. As solutions on the M_0 branch are unstable at its inception, techniques that allow continuation of unstable limit cycles are required before the Floquet analysis can be carried out. Continuation of the M branch solutions to lower Re (by using a stable solution as initial condition at lower Re) results in an evolution to the V branch. The hysteresis between the M and V branches was also observed in the experiments of Stevens *et al.* (1989).

The V solution branch, which is stable for the Reynolds number range 3250–3683, possesses the most interesting dynamical behaviour of the three identified branches. While the A and M branches can be readily associated with the first and third modes to bifurcate from the basic state as Reynolds number is increased (Lopez *et al.* 2001), the V branch is not so easily categorized. Its most likely genesis is as a mixed mode between the second and third modes to bifurcate from the basic state, since it always possesses some characteristics of the M branch, and appears to terminate with a bifurcation to the M branch at the upper Reynolds number limit. There may be similarities here with the mixed-mode behaviour that occurs near the onset of three-dimensional vortex shedding in a circular cylinder wake (Barkley, Tuckerman & Golubitsky 2000).

The distinguishing feature of the V branch is the very-low-frequency modulation; this is present for both the axisymmetric and non-axisymmetric cases, and has been observed experimentally (Stevens *et al.* 1999, figure 5). In the axisymmetric restriction, there appear to be three fundamental periods, only two of which are independent. Apart from the VLF, there are two periods which are close to a $1:2$ resonance, near $\Omega T_1 = 28$ and $\Omega T_2 = 57$. The T_1 component appears to be related to the M branch (which has $\Omega T = 28.3$ in the axisymmetric restriction), and from Lopez *et al.* (2001) $2\pi/T_1$ is very close to the imaginary part of the eigenvalues for the third Hopf bifurcation from the basic state. In addition, $2\pi/T_2$ is also close to the imaginary part of the eigenvalues of the second Hopf bifurcation from the basic state.

Flows of the V branch are axisymmetric near the middle of its Reynolds number range and lose stability to $P = 5$ azimuthal modes via supercritical Hopf-type bifurcations from the axisymmetric quasi-periodic state, again leading to MRWs, modulated at a VLF in addition to the higher frequencies. The precession rate of the MRWs remains constant near these bifurcations, with $\omega/\Omega = 0.132$, the same as for the M branch, and in addition the (z, r) location of the peak energy in the MRW has a very similar location and distribution as for the M branch solutions. The V_5 branch terminates at the upper Reynolds number of 3683, with $T_{\mathrm{mod}} \to \infty$ as it merges with the M_5 branch.

Modulated rotating waves with a VLF have previously been observed in the Taylor–Couette experiments of von Stamm *et al.* (1996). In addition, the quasi-periodic behaviour of the VLF MRWs became chaotic though a period doubling cascade (cascaded 'period-doubling-on-a-torus') with increasing Reynolds number. In the present work, we also appear to have observed the first two period doublings of such a cascade, on the lower Re limit of the V_5 branch, but in this case the period doublings occur as Reynolds number is reduced, and the 'cascade' terminates with a

return to the axisymmetric behaviour of the V_0 branch near $Re = 3283$ (or possibly, our initial value approach was not able to observe more period doublings, as the co-existing A branch may have a larger basin of attraction at these Re). It is curious that the first period doubling appears near the same Reynolds number as the T_{mod} cusp in the V_0 branch.

Rotating waves and modulated rotating waves are a common feature of bifurcations for flows with $SO(2)$ symmetry, and have received substantial attention through theoretical and experimental studies (Gorman & Swinney 1982; Rand 1982; Coughlin & Marcus 1992; von Stamm *et al.* 1996; Lamb & Melbourne 1999). Most of the past works have focused on flows in the Taylor–Couette system; in that system, the first unsteady behaviour as Reynolds numbers are increased is typically through an equivariant bifurcation to rotating waves, in which the flow is steady when viewed in an appropriate steadily rotating frame. It is only subsequent to this bifurcation that true unsteady behaviour appears through modulation of the RWs, or the appearance of a VLF, either of which are the precursor to chaotic behaviour. When modulations occur, these in general break the P-fold symmetry of the waves, although axisymmetric kinds can also occur (Gorman & Swinney 1982; Rand 1982). In the present study, we have outlined another scenario, whereby the time periodicity appears first in the axisymmetric mode, and then the axisymmetric limit cycle undergoes symmetry breaking directly to a modulated rotating wave, without an intermediate pure rotating wave state. The modulated rotating waves are never steady in any rotating reference frame. Hence, MRW states on the M branch can be regarded as 2-tori, while MRW on the V branch, where the axisymmetric state already has two independent frequencies, can be regarded as 3-tori. The V_5 state provides one of the very few examples of stable 3-tori solutions in laminar non-chaotic flow that have been observed experimentally (Stevens *et al.* 1999) and investigated in detail by computations of the three-dimensional Navier–Stokes equations, over an extensive range in Reynolds number.

We thank the staff of the Australian Partnership for Advanced Computing (APAC) National Facility, and the CSIRO–Bureau of Meteorology Joint High Performance Computing and Communications Centre (HPCCC) for their continued support and assistance. HMB acknowledges the support of the APAC Merit Allocation Scheme. JML acknowledges the support of the National Science Foundation (NSF), under grant CTS-9908599.

REFERENCES

Barkley, D., Tuckerman, L. S. & Golubitsky, M. S. 2000 Bifurcation theory for three-dimensional flow in the wake of a circular cylinder. *Phys. Rev.* E **61**, 5247–5252.

Batchelor, G. K. & Gill, A. E. 1962 Analysis of the stability of axisymmetric jets. *J. Fluid Mech.* **14**, 529–551.

Blackburn, H. M. & Graham, L. J. W. 2000 Vortex breakdown – theory and experiment. *Album of Visualization* **17**, 13–14.

Blackburn, H. M. & Lopez, J. M. 2000 Symmetry breaking of the flow in a cylinder driven by a rotating endwall. *Phys. Fluids* **12**, 2698–2701.

Chossat, P. & Lauterbach, R. 2000 *Methods in Equivariant Bifurcations and Dynamical Systems.* World Scientific.

Coughlin, K. T. & Marcus, P. S. 1992 Modulated waves in Taylor–Couette flow. Part 1. Analysis. *J. Fluid Mech.* **234**, 1–18.

Escudier, M. P. 1984 Observations of the flow produced in a cylindrical container by a rotating endwall. *Exps. Fluids* **2**, 189–196.

Gelfgat, A. Y., Bar-Yoseph, P. Z. & Solan, A. 1996 Stability of confined swirling flow with and without vortex breakdown. *J. Fluid Mech.* **311**, 1–36.

Gelfgat, A. Y., Bar-Yoseph, P. Z. & Solan, A. 2001 Three-dimensional instability of axisymmetric flow in a rotating lid–cylinder enclosure. *J. Fluid Mech.* **438**, 363–377.

Gerritsma, M. I. & Phillips, T. N. 2000 Spectral element methods for axisymmetric Stokes problems. *J. Comput. Phys.* **164**, 81–103.

Ghidersa, B. & Dŭsek, J. 2000 Breaking of axisymmetry and onset of unsteadiness in the wake of a sphere. *J. Fluid Mech.* **423**, 33–69.

Gorman, M. & Swinney, H. L. 1982 Spatial and temporal characteristics of modulated waves in the circular Couette system. *J. Fluid Mech.* **117**, 123–142.

Iooss, G. & Adelmeyer, M. 1998 *Topics in Bifurcation Theory and Applications*, 2nd Edn. World Scientific.

Karniadakis, G. E., Israeli, M. & Orszag, S. A. 1991 High-order splitting methods for the incompressible Navier–Stokes equations. *J. Comput. Phys.* **97**, 414–443.

Knobloch, E. 1994 Bifurcations in rotating systems. In *Lectures in Solar and Planetary Dynamos* (ed. M. R. E. Proctor & A. D. Gilbert), pp. 331–372. Cambridge University Press.

Kuznetsov, Y. A. 1998 *Elements of Applied Bifurcation Theory*, 2nd Edn. Springer.

Lamb, J. S. W. & Melbourne, I. 1999 Bifurcation from discrete rotating waves. *Arch. Rat. Mech. Anal.* **149**, 229–270.

Lopez, J. M. 1990 Axisymmetric vortex breakdown. Part 1. Confined swirling flow. *J. Fluid Mech.* **221**, 533–552.

Lopez, J. M., Marques, F. & Sanchez, J. 2001 Oscillatory modes in an enclosed swirling flow. *J. Fluid Mech.* **439**, 109–129.

Lopez, J. M., Marques, F. & Shen, J. 2002 An efficient spectral-projection method for the Navier–Stokes equations in cylindrical geometries II. Three dimensional cases. *J. Comput. Phys.* **176**, 384–401.

Lopez, J. M. & Perry, A. D. 1992 Axisymmetric vortex breakdown. Part 3. Onset of periodic flow and chaotic advection. *J. Fluid Mech.* **234**, 449–471.

Lugt, H. & Abboud, M. 1987 Axisymmetric vortex breakdown with and without temperature effects in a container with a rotating lid. *J. Fluid Mech.* **179**, 179–200.

Mamun, C. K. & Tuckerman, L. S. 1995 Asymmetry and Hopf bifurcation in spherical Couette flow. *Phys. Fluids* **7**, 80–91.

Marques, F. & Lopez, J. M. 2001 Precessing vortex breakdown mode in an enclosed cylinder flow. *Phys. Fluids* **13**, 1679–1682.

Marques, F., Lopez, J. M. & Shen, J. 2002 Mode interactions in an enclosed swirling flow: a double Hopf bifurcation between azimuthal wavenumbers 0 and 2. *J. Fluid Mech.* **455**, 263–281.

Orszag, S. A. 1974 Fourier series on spheres. *Mon. Weath. Rev.* **102**, 56–75.

Rand, D. 1982 Dynamics and symmetry. Predictions for modulated waves in rotating flows. *Arch. Rat. Mech. Anal.* **79**, 1–38.

Rønquist, E. M. 1988 Optimal spectral element methods for the unsteady three-dimensional incompressible Navier–Stokes equations. PhD thesis, Massachusetts Institute of Technology.

Shen, J. 1997 Efficient spectral–Galerkin methods III: polar and cylindrical geometries. *SIAM J. Sci. Comput.* **18**, 1583–1604.

Sørensen, J. N. & Christensen, E. A. 1995 Direct numerical simulation of rotating fluid flow in a closed cylinder. *Phys. Fluids* **7**, 764–778.

von Stamm, J., Gerdts, U., Buzug, T. & Pfister, G. 1996 Symmetry breaking and period doubling on a torus in the VLF regime in Taylor–Couette flow. *Phys. Rev.* E **54**, 4938–4957.

Stevens, J. L., Lopez, J. M. & Cantwell, R. J. 1999 Oscillatory flow states in an enclosed cylinder with a rotating endwall. *J. Fluid Mech.* **389**, 101–118.

Tomboulides, A. G. & Orszag, S. A. 2000 Numerical investigation of transitional and weak turbulent flow past a sphere. *J. Fluid Mech.* **416**, 45–73.

Tsitverblit, N. 1993 Vortex breakdown in a cylindrical container in the light of continuation of a steady solution. *Fluid Dyn. Res.* **11**, 19–35.

Tuckerman, L. S. 1989 Divergence-free velocity fields in nonperiodic geometries. *J. Comput. Phys.* **80**, 403–441.

Vogel, H. U. 1968 Experimentelle Ergebnisse über die laminare Strömung in einem zylindrischen Gehäuse mit darin rotierender Scheibe. *Tech. Rep.* 6. Max-Planck-Inst.